The influence of surface roughness and high pressure torsion on the growth of anodic titania nanotubes on pure titanium

Nan Hu，Nong Gao and Marco J. Starink

Engineering Materials group, Faculty of Engineering and the Environment，University of Southampton, SO17 1BJ, UK

Abstract

Anodic titanium dioxide nanotube (TNT) arrays have wide applications in photocatalytic, catalysis, electronics, solar cells and biomedical implants. When TNT coatings are combined with severe plastic deformation (SPD), metal processing techniques which efficiently improve the strength of metals, a new generation of biomedical implant is made possible with both improved bulk and surface properties. This work investigated the effect of processing by high pressure torsion (HPT) and different mechanical preparations on the substrate and subsequently on the morphology of TNT layers. HPT processing was applied to refine the grain size of commercially pure titanium samples and substantially improved their strength and hardness. Subsequent anodization at 30 V in 0.25 wt. % NH_4F for 2 hours to form TNT layers on sample surfaces prepared with different mechanical preparation methods was carried out. It appeared that the local roughness of the titanium surface on a microscopic level affected the TNT morphology more than the macroscopic surface roughness. For HPT-processed sample, the substrate has to be pre-treated by a mechanical preparation finer than 4000 grit for HPT to have a significant influence on TNTs. During the formation of TNT

layers the oxide dissolution rate was increased for the ultrafine-grained microstructure formed due to HPT processing.

Key words:

Titania nanotubes; Anodization; High pressure torsion; Sample preparation; Mechanical grinding and polishing.

1 Introduction

Titanium and its alloys are widely used in biomedical implants [1, 2], because of their good mechanical and surface properties. Although the success rate of titanium implants is very high [3], failures do happen due to various factors. Overloading and insufficient osseointergration are complications related with the implant material that demand solutions from materials science. To address overloading, processing titanium through severe plastic deformation (SPD), such as high pressure torsion (HPT) [4], can increase hardness and strength whilst maintaining good ductility without introducing harmful or costly additional elements [5]. In addition, modifying the natural oxide layer of titanium, which provides remarkable surface properties, can address issues related to insufficient osseointegration [6] and undesired cell growth [7-9]. Titanium dioxide nanotubes (TNT) made by electrochemical anodization can modify the oxide layer, which can be utilized to positively affect cellular behaviours, such as migration [9], adhesion [10], proliferation [7, 10, 11] and differentiation [12, 13]. By modifying the surfaces of SPD processed titanium with TNT layers, there is a possibility to simultaneously increase the bulk and surface properties, therefore further increasing the success rate of titanium implants. The present work is the first time that the anodization behaviour of SPD processed titanium is being investigated.

A typical characteristic of ultra-fine-grained (UFG) materials made by SPD processing is their high density of lattice defects, including vacancies, dislocations, grain boundaries as well as other types of defects [4]. Grain boundaries are usually associated with an increased electrical resistivity and enhanced atom diffusivity, which may lead to a different electrochemical behaviour, such as anodization and corrosion. However, although they have shown some unusual corrosion behaviours [14-17] compared to titanium in normal grain size, the anodization behaviours of UFG titanium made by SPD processing have rarely been investigated. To further understand the influence of grain refinement on anodization, a study on the anodization mechanisms of UFG titanium produced by SPD is needed.

In addition, most researches aiming to control the morphology and properties of TNT layers mainly focused on tailoring the extrinsic parameters, i.e. electrochemical parameters such as potential [18], electrolyte types [19-22], water content [23] and sweep rates [24]. However, the influence of intrinsic factors, such as surface roughness, surface conditions and grain size and orientation of the titanium substrate are rarely studied [25-28] and the significant influence of sample preparation methods on TNT growth makes it difficult to study the effects of grain size separately [27, 28]. Lu et al. [27] anodized samples with various surface conditions: as-received, chemical polished, mechanical polished and electropolished states and found that the morphologies of TNT layers on these four kinds of samples are quite different from each other. But another study using the same set of samples showed very different nanotube growth and morphologies [28]. In this work, one aim is to find out the proper sample preparation to reveal the influence of substrate microstructure on the growth of TNT layers. Therefore titanium surfaces with different surface roughness prepared only by mechanical grinding or polishing were used in anodization, so they only differ in surface roughness with similar surface chemical composition and surface oxide layer. Another aim of this study is to explore the influence of HPT processing on the TNT layers for the new

generation of biomedical materials. Titanium samples in two different grain sizes: UFG titanium prepared by HPT and coarse-grained titanium were used. Since TNTs also have wide applications in other areas such as photocatalytic devices [29], electronics [30], solar cells [31] and sensors [32], a study of the anodization behaviour of UFG titanium may also provide insights relevant for these applications.

2 Experimental

In this study, commercially pure (CP) titanium (Grade 2) was used. Before HPT processing, CP Ti extruded bars with a diameter of 10 mm were cut and ground into slices with thickness between 0.80 ~ 0.85 mm. The slices annealed at 750 ℃ for 30 minutes were designated as coarse-grained (CG) samples. The mechanism for HPT processing is illustrated in Figure 1 [33]. The experiment was carried out under a quasi-constrained condition, using two anvils under an imposed pressure, *P*. Torsional straining was applied through rotation of the lower anvil. HPT processing was carried out under 3 GPa pressure with 10 turns at room temperature.

A Matsuzawa Seiki MHT-1 microhardness tester was used to measure the Vickers micro-hardness, Hv, of the samples. All the samples were ground with SiC abrasive papers from 120, 800, 1200 and to 4000 grit successively before the hardness test. All the tests were carried out under a weight of 1000 g at a dwell time of 15 s. The tensile tests were performed on an Instron 3300 testing system with a load resolution of 0.1 N. Small tensile specimens with a 1 mm gauge length and 1 mm width were machined from HPT disks using electro-discharge machining. The ultimate tensile strength (UTS) was obtained from the tensile curve and the percentage elongation was calculated by using the elongated length of the gauge after fracture.

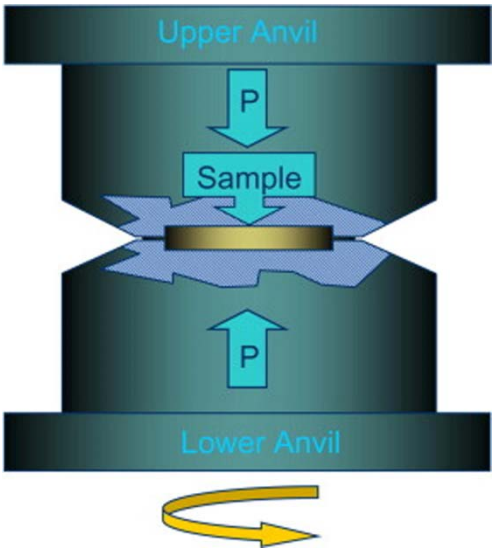

Figure 1 Schematic illustration of the HPT facility [33].

An Olympus BX41M-LED microscope was used for optical microscopy (OM) observation to measure the grain size of the CG sample. Samples were ground with SiC abrasive papers of 120, 800, 1200 and 4000 grit, and then polished with 6 μm and 1 μm diamond paste (Struers). After grinding and polishing, etching with an acid solution containing HF, HNO_3 and H_2O with a volume percentage of 2:3:10 was conducted. A linear intercept method was used for measuring grain size in OM images. A U-AN360-3 polarizer was used to make coloured metallographic images with polarized light.

A JEM 3010 Transmission Electron Microscope (TEM) was used for TEM observation with an accelerating potential of 300 kV. TEM samples were prepared through twin-jet electropolishing with a solution containing 6% $HClO_4$ + 4% H_2O+ 90% ethanol under 30 V at a temperature between -30 to -25 ℃. Selected area electron diffraction (SAED) was carried out with a spot size of 360 nm. X-ray diffraction (XRD) analysis was conducted using a Bruker D2 PHASER diffractometer equipped with a graphite monochromator using Cu *K*α radiation.

Prior to anodization, both CG and HPT samples were subjected to five types of mechanical pre-treatments: grinding with 120, 800, 1200 and 4000 grit abrasive papers and polishing with 1 μm diamond paste. The grits are determined from European FEPA or P-Grading standard, and particle sizes for the five treatments are 125, 22, 15, 5 and 1 μm, respectively. In this paper, the 1 μm polished state will be referred to as the equivalent grit size, i.e. a 14000-grit state. After grinding and polishing, each sample was ultrasonicated in acetone for 15 minutes and in distilled water for 15 minutes, respectively, therefore it is expected that no particles are left on the sample surface before anodization.

After each mechanical preparation, the processed surface profiles were recorded using infinite focus optical microscopy (IFM) on an Alicona non-contact profilometer. A total of five measurements were made per sample to allow calculation of mean and standard deviation. The ASME B46.1-2002 standard was used to calculate the surface roughness of these ground samples. For the 14000-grit sample, the surface roughness (*R*a) was tested on a Taylor-Hobson facility. In this investigation, data for every measurement was collected from a length of 5 mm travelled by a stylus, which records the profile information. Each sample was tested four times and the average *R*a was obtained from these measurements.

Anodization was carried out on a two-electrode cell to fabricate TiO_2 nanotubes on the surface of titanium samples. In this work, an organic based electrolyte containing 0.25 wt. % ammonium fluoride (Riedel-de Haën), 1 wt. % deionized water and 98.75 wt. % glycerol (Alfa Aesar) was used. Ti samples were anodes of the cell with a round area of diameter of 0.6 mm exposed to the electrolyte. The dimensions of those anode samples are identical to the HPT sample: disk with a diameter of ~ 10 mm and thickness of ~ 0.6 mm. Constant direct currents of 30 V or 15 V were used. The distance between electrodes was 1 cm, and all the anodization experiments lasted for 2 hours. The current density vs. time transient curves (*j*-*t* curves) were recorded. CG samples anodized under 30 V are labelled as CG30 followed by

grit numbers and those anodized under 15 V are labelled as CG15 followed by grit numbers. HPT samples anodized under 30V are labelled as HPT30 followed by grit numbers. Thus anodization was performed on 15 different samples and the labels of those samples are presented in Table 1.

Table 1 Labels of samples in different grain size and surface roughness anodized at different potentials

	120 grit	**800 grit**	**1200 grit**	**4000 grit**	**14000 grit**
CG at 30 V	CG30-120	CG30-800	CG30-1200	CG30-4000	CG30-14000
CG at 15 V	CG15-120	CG15-800	CG15-1200	CG15-4000	CG15-14000
HPT at 30 V	HPT30-120	HPT30-800	HPT30-1200	HPT30-4000	HPT30-14000

The morphology of the titania nanotubes was observed on a Jeol JSM 6500F field-emission SEM. Secondary electrons under accelerating potential of 10 kV were used for the observation. Nano Measurer 1.2 software was used to measure the nanotube morphologies including top and bottom diameters, and TNT layer thickness.

3 Results and analysis

3.1 Substrate characteristics before anodization

3.1.1 The microstructure and properties of titanium substrates

Figure 2(a) shows the polarized light image of the CG sample, the different colours are due to different orientations of the grains. The mean grain size for the CG sample is 13 ± 2 μm. Figure 2 (b) shows the microstructure of samples subjected to 10 turns of HPT processing. No clear grain boundaries can be seen indicating grain sizes are smaller than the resolution. Therefore, it is necessary to use TEM with much better resolutions to study the

microstructures of HPT-processed samples. Figure 2 (c) shows a bright field TEM image of the HPT-processed sample, and (d) is the corresponding dark field image. The in-set image is the SAED pattern of the blue circled area in Figure 2 (c) with a spot size of 360 nm. It can be seen from these TEM images that the microstructure is reasonably homogenous and grain size had been refined to nano-scale after HPT processing. Even with a small aperture size of 360 nm, the diffraction pattern still presents lots of spots arranged in circles, indicating several grains with high angle grain boundaries exist in this small area [5]. In addition, the significant spreading of spots confirms the existence of high microstrains [34]. The existence of high microstrains is also confirmed by XRD peak broadening presented in the supplementary data (Figure 1S), from which we have derived a microstrain of ~ 0.19 % and a dislocation density of ~ 4.6×10^{14} m^{-2}. The non-uniform contrast in bright-field and dark-field images also indicates significant distortions. From the dark field image, the average grain size of the HPT processed sample was estimated as 140 ± 10 nm. The results of microhardness and tensile tests show that the Hv and UTS have been significantly increased from 1.7 GPa and 580 MPa in the CG sample to 2.8 GPa and 860 MPa in the HPT sample.

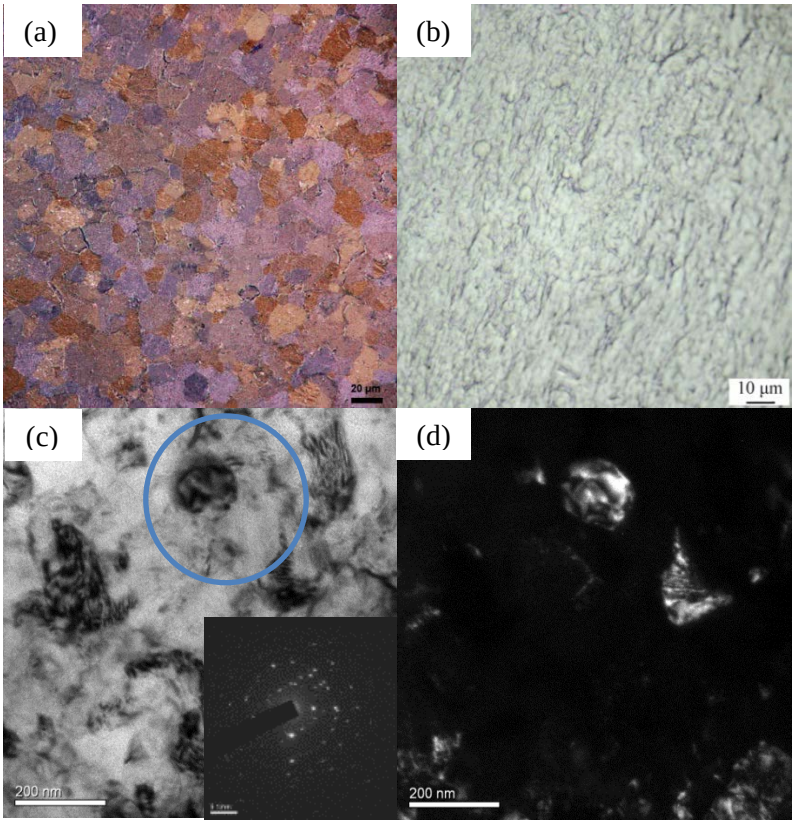

Figure 2 OM images of titanium substrates: (a) the CG sample, (b) the HPT sample. TEM images of the HPT sample: (c) bright-field (SAED as an inset) and (d) the corresponding dark-field image.

3.1.2 Surface roughness before anodization

Figure 3 shows CG Ti sample surfaces after surface preparations with various mechanical preparations. The insets show the IFM data with pseudo colours representing height. Generally, with the increase of grit numbers, R_a decreases. The depth of maximum scratch grooves decreases from more than 2 µm in the 120 grit sample (Figure 3 (a)) to about 100 nm in the 14000 grit sample (Figure 3 (e)). Ground HPT-processed samples show a surface topography similar to the CG samples.

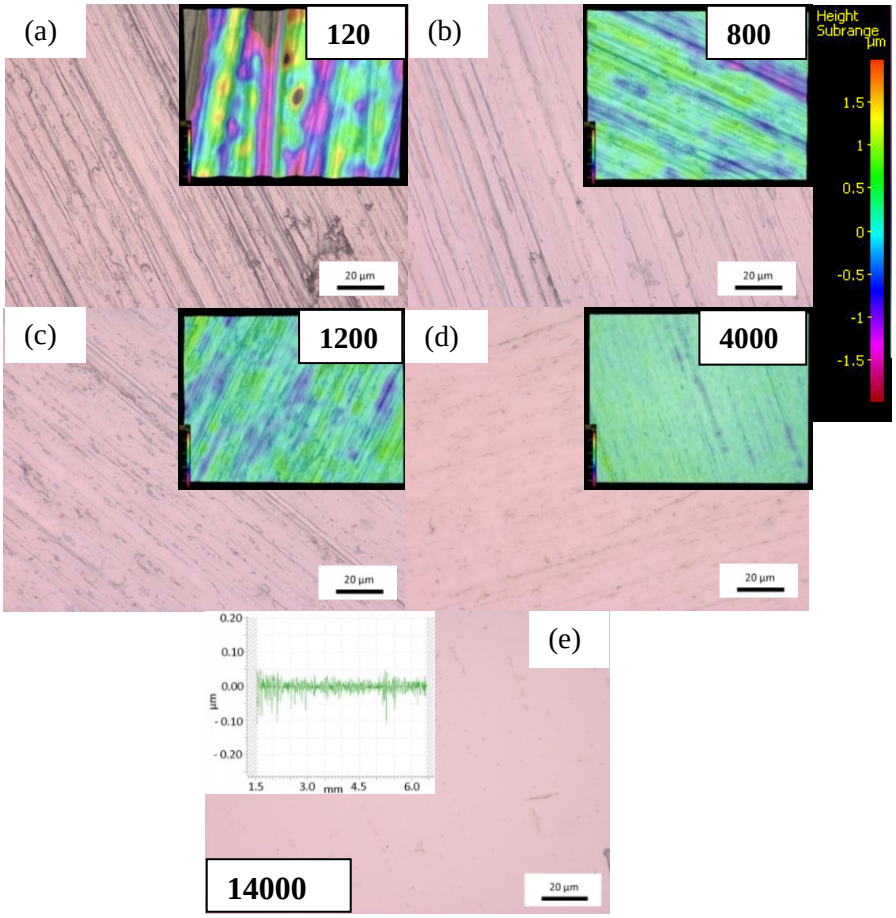

Figure 3 OM surface images and topographies prior to anodization. The insets are the corresponding Alicona IFM images where each colour represents a different height. Surfaces respectively ground by (a) 120, (b) 800, (c) 1200, and(d) 4000 grit abrasive paper. (e) Surface polished by 14000 grit diamond paste.

In order to view effects of different mechanical preparations at a scale relevant to TNTs (which have a diameter of several tens of nm), analysis of the CG sample surfaces are conducted in SEM, illustrated in Figure 4. The 120, 800 and 1200 grit samples show similar surfaces in SEM images (Figure 4 (a-c). Taking the 800 grit sample as an example, the lower left half of the image in Figure 4 (b) is part of a scratch with the linear feature near the diagonal of the image being the edge of the scratch. Except for the rough scratch edge area, the surface within the scratch is comparatively smooth and many nanotubes can form within a

locally “smooth” surface at the bottom of a scratch. In this image, the width of the crack edge is about 100 nm, so the percentage of the “rough” scratch area in the image is about 10.8%. Although the 4000 grit sample is smoother in terms of the macroscopic R_a, the magnified SEM image shows that it is actually much rougher (Figure 4 (d)), containing more irregularities at the scale of the nanotube diameters (~30-80 nm). The area within the scratch is rough and rippled therefore can be regarded as a locally “rough” area while the surface outside of the scratch is smooth. So in the 4000 grit sample, the percentage of the rough scratch area is about 28 % in Figure 4 (d). For the 14000-grit sample, the majority of the surface is smooth with only a very small scratch seen in Figure 4 (e). The width and length of the scratch is about 80 and 100 nm. The percentage of the scratch on the surface is about 0.2 % in this image.

3.2 TNT Growth mechanisms for substrates in different roughness and grain sizes

The current density vs. anodization time, *j*-*t*, transient curves for samples subjected to different mechanical preparations are shown in Figure 5, which demonstrates that mechanical preparations lead to three types of curves:

(i) Typical *j*-*t* curves: 120, 800 and 1200 grit samples

The 120, 800 and 1200 grit samples in Figure 5 show typical features of *j*-*t* curves with three stages (I, II and III) [35] during the formation of TNT layers [36, 37].

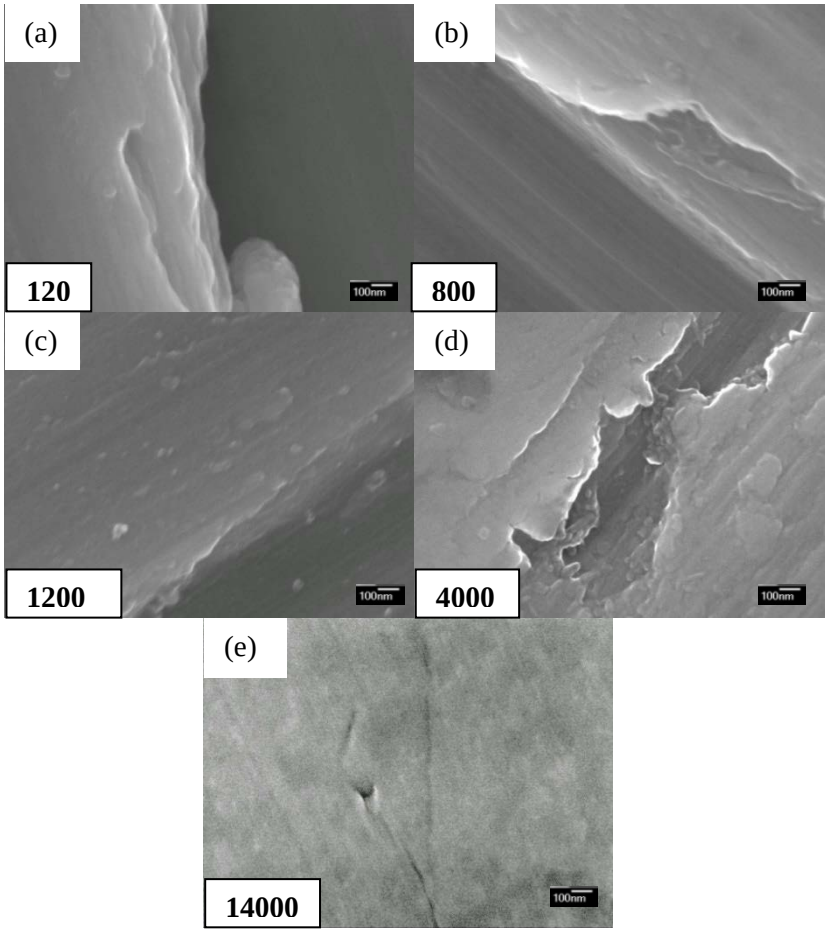

Figure 4 SEM images of CG sample substrates processed by (a) 120, (b) 800, (c) 1200 and (d) 4000 grit abrasive paper. (e) Surface polished by 14000 grit diamond paste before anodization.

For CG samples anodized at 15 V, the 120, 800 and 1200 grit samples showed similar three-stage behaviour as those anodized at 30 V but at about half the magnitude of *j*. The transition points between stages are quite similar for CG samples anodized at 30 V and 15 V.

HPT samples anodized at 30 V show similar trends as CG samples in the same anodization conditions. For surfaces pre-treated by 120, 800 and 1200 grit abrasive papers, little difference is found between TNT layers on CG and HPT samples.

(ii) The lowest current density: 4000 grit samples

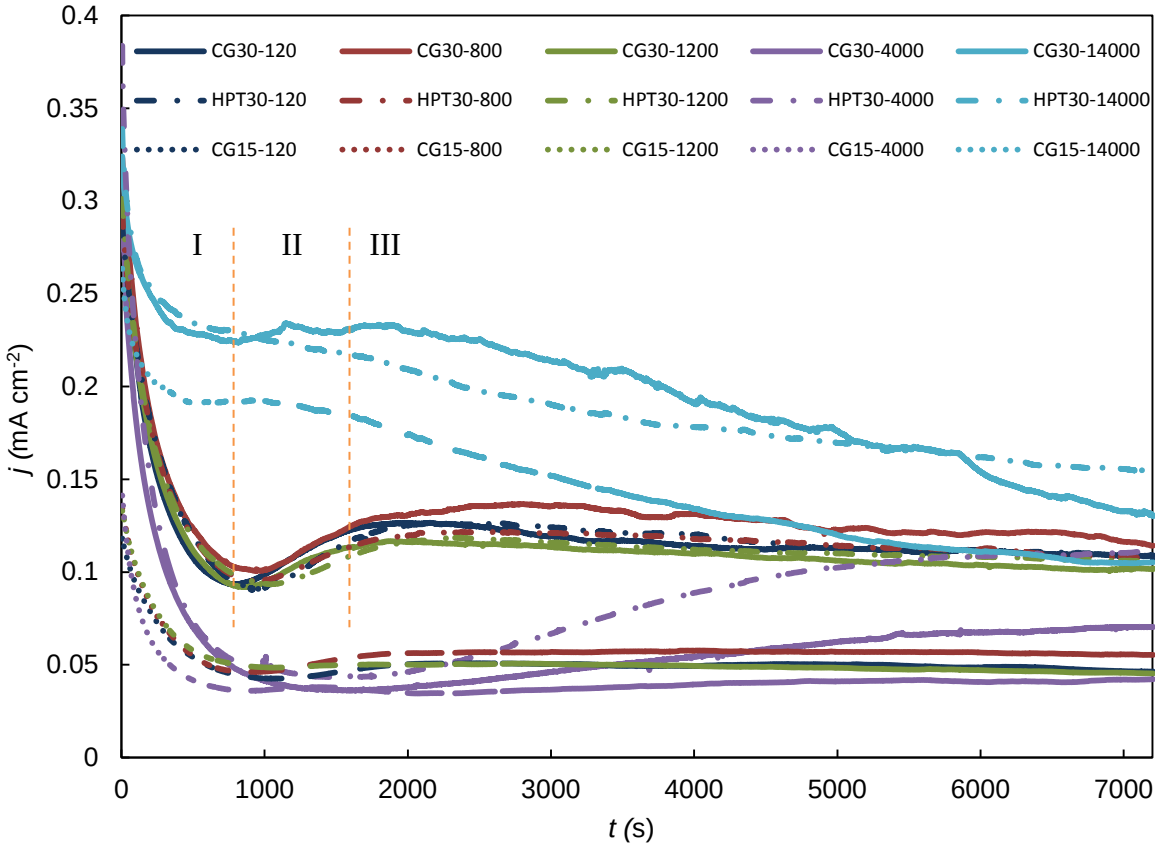

Figure 5 The *j*-*t* curves for CG samples at 30 V (solid lines) and 15 V (round dot line) and for HPT samples at 30 V (dash dot line).

Samples with smoother surfaces (4000 and 14000 grit samples) show trends that are distinctively different from the typical ones discussed above. The *j*-*t* curve of the CG30-4000 sample also shows the three-stage behaviour, but with a much lower *j* than that of all the other samples. Moreover, the CG30-4000 sample shows an extended time period in Stage I and II compared to the CG30-800 sample, which indicates that the nucleation rate of TNTs on the CG30-4000 sample is much slower than that of the CG30-800 sample. Moreover, the HPT30-4000 sample showed a higher *j* and comparatively short time period in Stage I and II compared to the CG30-4000 sample and the former shows a Stage III while the latter does not. Since HPT30-4000 sample showed the same oxidation rate as the CG30-4000 sample in

Stage I, the difference between them in Stage II and III can be explained by a quicker oxide dissolution rate on the HPT sample.

(iii) The highest current density: 14000 grit samples

The CG30-14000 and the CG15-14000 sample show the typical three-stage trend but at a much higher *j* compared to the four samples with rougher surface conditions in the same anodization condition. For the HPT30-14000 sample, although it shows a similar *j* to the CG30-14000 sample, it is difficult to distinguish Stage I, II and III on the *j*-*t* curve. One simply observes a monotonic decrease of *j* along the whole anodization period on the HPT sample.

3.3 TNT morphologies

Figure 6 (a) to (e) shows the top surface morphologies of TNT layers on the CG Ti samples anodized at 30 V. On the surface of all the TNT layers a layer of capping oxides is found, which is a remnant of the penetration of the compact oxide formed in Stage I, and this capping oxide layer is frequently found on the nanotube tops after anodization [36]. The dimensions of the TNT layers underneath the capping oxide are shown as the insets in Figure 6 (a)-(e), and the internal diameter (d_{in}) and external diameter (d_{ex}) of the nanotubes are illustrated in Figure 6 (f). The 120, 800 and 1200 grit samples display similar TNT dimensions with d_{in} of 22-26 nm and d_{ex} of 61-65 nm. The size of nanotubes on the 4000 grit sample (Figure 6 (d)) is larger than that on the 800 grit sample (Figure 6 (b)) with the former having d_{in} of ~16 nm, d_{ex} of ~77 nm. On the 14000 grit sample d_{in} is ~17 nm and d_{ex} is ~26 nm.

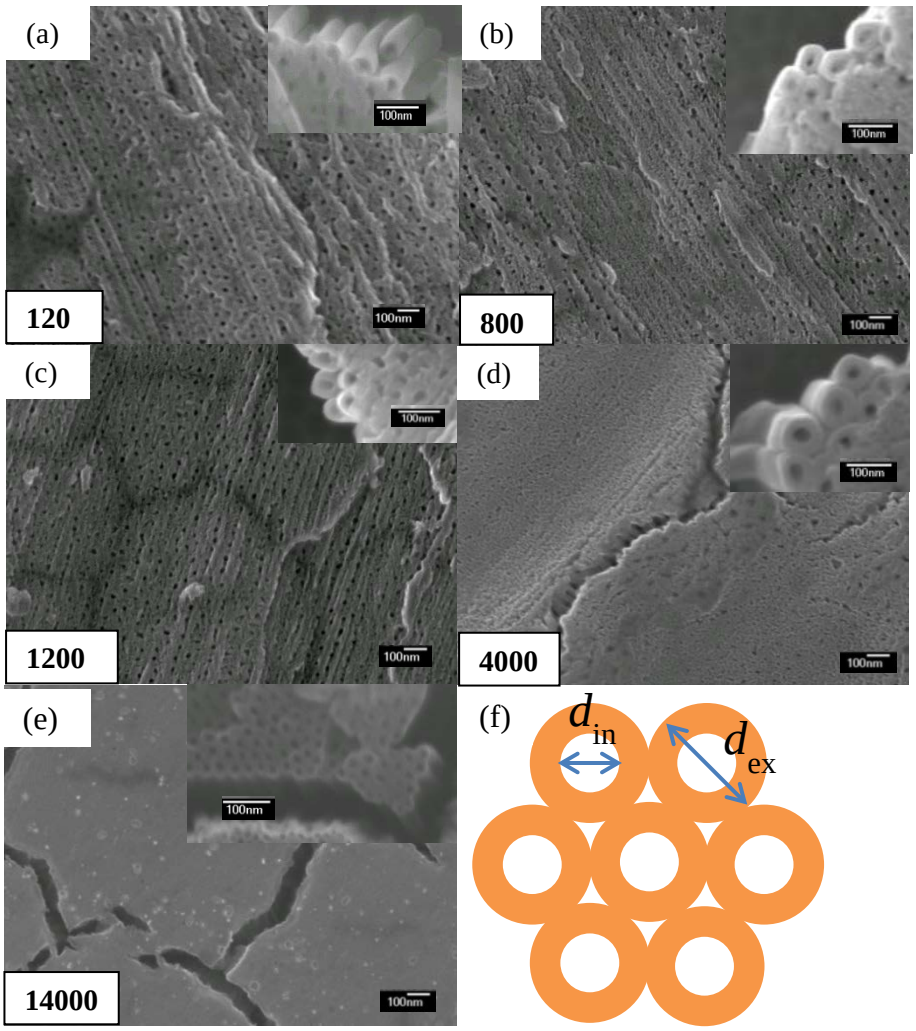

Figure 6 SEM top views of the TNT layers on CG samples after 2 h of anodization under 30 V: (a) 120, (b) 800, (c) 1200, (d) 4000 and (e) 14000 grit samples, and (f) is a schematic depiction of the morphology of TNTs in the insets. The insets in (a-e) show the corresponding top views of TNTs after removing the capping oxide.

To further investigate the influence of R_a on the TNT growth, the layers of anodized nanotubes were peeled off from the Ti substrate on the CG 800, 4000 and 14000 grit samples to reveal the bottom morphologies of TNTs (Figure 7). The CG 120, 800 and 1200 samples show similar *j-t* curves (Figure 5) and SEM images (Figure 6 (a)-(c)), therefore one sample (CG30-800) is selected as the representative of these three samples shown in Figure 7 (a). The insets in Figure 7 are the TNT bottom morphologies on HPT samples with the same

surface condition. Whilst at the top the TNT layer is covered by a capping oxide layer, which makes the observation of nanotube spacing very difficult, at the bottom a fairly regular arrangement of nanotubes can clearly be seen. The approximately hexagonal type of alignment of TNTs are marked by red hollow hexagons in Figure 7 (a)-(c). The schematic image of the ideal arrangement of TNTs at the bottom with the illustration of bottom diameter (d_{bt}) and the inter-tube distance (i_d) is shown in Figure 7 (d).

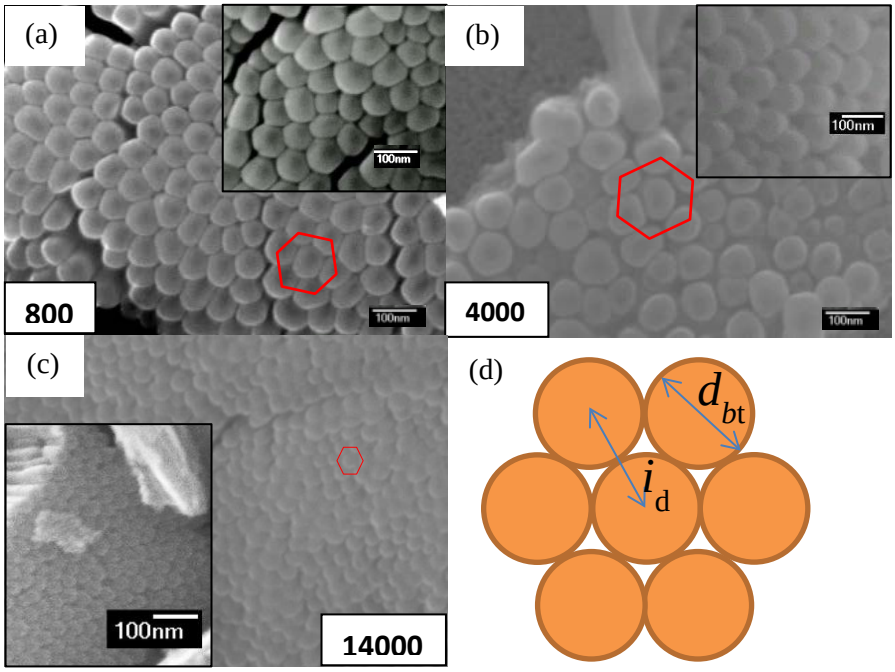

Figure 7 SEM images of the bottom of TNT layers on different surface conditions on CG samples anodized at 30 V: (a) 800, (b) 4000 and (c) 14000 grit samples, and (f) is a schematic depiction of the bottom of TNT layers. The insets show the bottom of TNT layers on HPT sample with the same surface condition.

Figure 7 (a) shows that the bottom of nanotubes on the CG 800 grit sample is comparatively homogeneous with a d_{bt} of ~ 70 nm. And the HPT 800 grit sample showed very similar bottom dimensions. The CG 4000 grit sample, however, shows a different morphology: the size is much more inhomogeneous with the smallest diameter of ~ 40 nm and the largest up to ~100 nm and the average d_{bt} is ~75 nm with a larger spacing between single nanotubes.

The HPT 4000 grit sample showed an even larger d_{bt} of 90 nm and the CG 14000 grit sample shows the smallest d_{bt} of 40 nm as compared to other CG samples. The diameter is homogeneous and TNTs are close to each other with i_d of 40 nm. The HPT 14000 grit sample also showed the smallest d_{bt} compared with other HPT samples, with a size even smaller than that of the CG 14000 grit sample of 37 and i_d is 37 nm. The measurements of TNT bottom imensions at different surface condition on samples with different grain sizes is given in Table 2.

Table 2 TNT bottom dimensions at different surface condition on samples with different grain size

sample	**TNT dimension**	**800 grit**	**4000 grit**	**14000 grit**
CG	d_{bt}	70 nm	75 nm	40 nm
	i_d	68 nm	89 nm	40 nm
HPT	d_{bt}	70 nm	90 nm	37 nm
	i_d	69 nm	88 nm	37 nm

Figure 8 shows the characteristic dimensions of the nanotubes, including d_{ex}, d_{in} and d_{bt}, on CG samples processed by different mechanical preparation after anodization at 30 V. The CG 4000 grit sample shows the largest and the CG 14000 grit sample shows the smallest d_{ex} and d_{bt}. The 120, 800 and 1200 grit samples show diameters which lie in the middle. The relationship between R_a and nanotube diameter is complex: with the surface getting smoother, d_{ex} and d_{bt} firstly increases (4000 grit) and then decreases (14000 grit). For HPT samples, the same trend was found.

Figure 9 shows the thickness of TNT layers on the CG 800, 4000 and 14000 grit samples, in which the insets are the magnified cross-sectional images of the capping oxide layer at the top. The thickness of TNT layers on the CG 800, 4000 and 14000 grit samples are 797, 611

and 648 nm, respectively, and thicknesses of their capping oxide layers (t_c) are about 49, 115 and 42 nm. For the CG 800 and the 14000 grit samples, each nanotube touches adjacent ones in the cross-sectional view, whilst for the CG 4000 sample some neighbouring nanotubes appear separated but connected by “hair-like” structures (marked by a black arrow in Figure 10(b)). This is consistent with the bottom SEM images, in which nanotubes in the CG 800 and 14000 grit samples are closely connected to each other whilst there are some spaces between nanotubes on the CG 4000 grit sample.

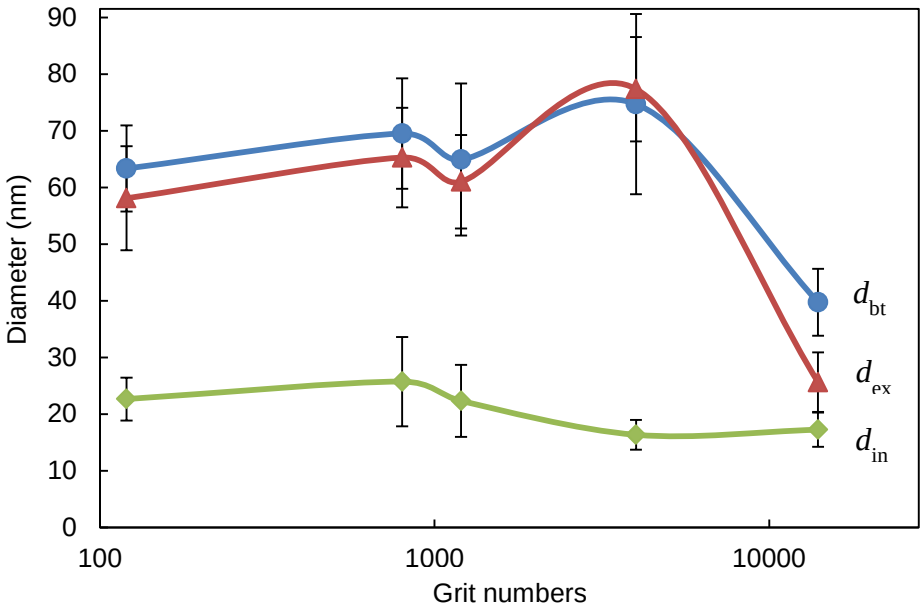

Figure 8 The characeristic sizes d_{bt}, d_{ex}, and d_{in} of CG samples on different surface conditions.

4 Discussion

4.1 The influence of HPT processing on the mechanical properties of CP titanium

Figure 2 shows that the grain size of CP titanium has been substantially refined from ~13 μm to ~ 140 nm after HPT processing. (It should be noted that grain sizes measured from dark field images can slightly underestimate the grain size due to distorted layers at the periphery of each grain [5].) The HPT processed Ti has large grain boundary misorientations [38], confirmed by a large number of well-spaced spots in a circle arrangement in the SAED patterns (Figure 2 (c) inset).

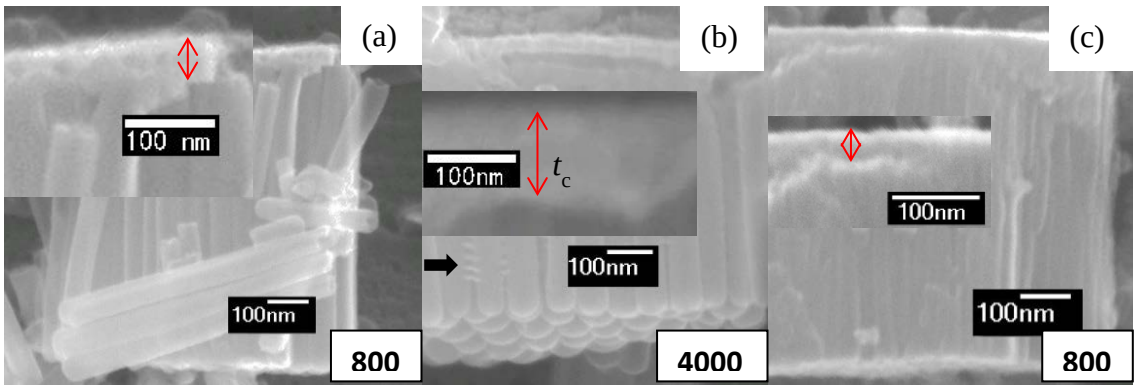

Figure 9 SEM images of the cross-sectional views of TNT layers on CG samples anodized at 30 V with different surface condition: (a) 800, (B) 4000 and (c) 14000 grit samples. The insets show the magnified images of the cross-section views of the capping oxide layer.

Most SPD-processed materials demonstrate enhanced hardness and strength at room temperature [39]. For conventional polycrystalline metals, the relationship between the strength as well as the hardness and the mean grain size can often be described by a Hall-Petch relationship [40]:

$$\sigma_y = \sigma_0 + kd^{-\frac{1}{2}} \qquad (1)$$

Where σ_y is the yield stress or the hardness, d is the average grain size, σ_0, and k are material constants. Table 3 summarizes the mechanical properties and grain sizes of CP Ti obtained in this work and in the literature with different SPD processing (including equal-channel angular pressing (ECAP)). It can be seen that after HPT processing, the grain size of CP titanium are all substantially refined and the UTS and Hv values are all improved with fair ductility. The main mechanism involved in grain boundary strengthening is the build-up of dislocations [39, 42, 43] at grain boundaries during deformation, and a detailed analysis of dislocation density and grains size data shows [39] that dislocation hardening is the main factor determining the improvements in strength in many SPD-processed pure and CP metals [42, 43], including Ti.

4.2 The influence of mechanical preparation on the morphologies of TNTs

The reasons for the complex relationship between TNT size and sample preparation methods (shown in Figure 8) can be illucidated by careful examinion of the *j*-*t* curves, as the size of TNTs is a result of the competition between oxide formation and dissolution, which is reflected in those curves. The present results show that both d_{ex} and d_{bt} decrease with increasing *j*. For example, the CG30-14000 grit sample shows the highest *j* in Figure 5, and in Figure 7 (c) it shows the smallest d_{bt}. For the CG30-4000 sample the inverse is the case. In work on anodized CP Ti samples prepared by different polishing methods [27], a similar trend was reported (samples displaying higher *j* during anodization showed smaller TNT diameters). However when different *j* values were achieved by changing the electrochemical settings such as the applied potential *U*, the diameter of TNTs was controlled by *U*, showing an opposite trend: the diameter increases with the increasing *j* and increases linearly with *U* [44, 45]. The applied potential *U* is widely accepted to control the nanotube size [10, 18, 44, 45]. In the current study, compared with the trend of d_{ex} and d_{bt}, the change of d_{in} on different surfaces is small (Figure 8) suggesting that *U* determines d_{in} of TNTs in

anodization, because all the samples with different R_a were anodized at the same U and they show similar d_{in}, therefore R_a has little influence on $d_{in.}$ However, the findings in this work indicate the macroscopic and microscopic surface roughness of titanium samples influences d_{ex} and d_{bt} of TNTs.

The difference in the d_{bt} and d_{ex} is atributed to their different j during anodization. In Stage I, a high resistance compact oxide layer is formed following the reaction [37]:

$$Ti + 2H_2O \rightarrow TiO_2 + 4H^+ + 4e^- \quad (2)$$

As the potential U is constant, the electric field $F=U/\delta_b$ decreases continuously with increasing thickness of oxide δ_b, leading to a drop of current (Figure 5) and j is related to the thickness of the compact oxide layer δ_b as [28]:

$$j = \alpha e^{\beta\frac{U}{\delta_b}} \quad (3)$$

where α and β are electrolyte and material dependent constants. From Eq. (3), it can be seen that a thick TiO_2 barrier layer δ_b will cause a low j. In Figure 5, the value of j from the lowest to the highest are on the CG30-4000, CG30-800 and CG30-14000 samples, respectively, therefore their δ_b after Stage I will decrease in that order. The value of t_c at the top of TNT layers after the anodization process, also supports this relation (Figure 9), because this capping oxide layer seen at this stage is the penetrated compact oxide layer formed in Stage I [24], therefore the value of t_c shows the value of δ_b when TNTs started nucleation. From Figure 9, t_c for the CG30-4000, CG30-800 and CG30-14000 samples are about 115, 49 and 42 nm, respectively.

In Stage I, δ_b is determined by field-aided transport of mobile ions (Ti^{4+}, OH^- and O^{2-}) through the oxide layer under a constant U. The efficient electric field across δ_b: $F_o=U/\delta_b$ drops constantly with increasing δ_b [37]. After Stage I, in order to maintain the oxidation

process, ions (i.e. O^{2-}, OH^-, Ti^{4+}, F^-) must move quickly through the oxide layer and porosity is induced due to the presence of F^- [37]:

$$TiO_2 + 6F^- + 4H^+ \rightarrow [TiF_6]^{2-} + 2H_2O \quad (4)$$

Similar to the case of oxide formation, the oxide dissolution is also determined by field-aided F^- migration, therefore the electric field for oxide dissolution also decreases with increasing δ_b : $F_d = U/\delta_b$. From Eq (3) we obtain:

$$F_d = \frac{\ln(\frac{j}{\alpha})}{\beta} \quad (5)$$

Since the CG30-14000 sample demonstrated the highest *j*, oxide dissolution on this sample is the strongest (highest F_d), leading to more breakdown sites which are the nuclei for TNT initiation and causing a faster initiation rate of TNTs. Therefore, on the CG30-14000 sample, TNT nucleation occurs at the fastest rate, leading to the smallest d_{ex} and d_{bt}. In contrast, on the CG30-4000 sample, which shows the lowest *j* at the end of Stage I and thus the weakest F_d, TNT nucleation occurs at the slowest rate, leading to the largest d_{ex} and d_{bt} and a prolonged nucleation time. Therefore, in this study, a high *j* at the end of Stage I results in small d_{ex} and d_{bt}.

The above rationalises the relation between *j* and d_{ex} and d_{bt}. The difference in the *j* of the different samples is thought to be caused by the surface morphology of those samples and particularly the microscopic surface roughness. Although the macroscopic surface roughness of titanium samples decreases with the increase of grit numbers (Figure 3), from Figure 4 it can be seen that the CG30-4000 sample is locally the roughest, followed by the CG30-800 sample and the locally smoothest CG30-14000 sample. The locally rough areas may act as nucleation sites for the oxidation process. The larger the percentage of rough areas, the higher the oxidation rate on the surface, leading to a lower *j* and a higher δ_b at the end of Stage I. This interpretation is supported by their measured *j* at the end of Stage I (Figure 5).

4.3 The influence of substrate grain size on the TNT layers

4.3.1 Surface preparation required to reveal the influence of substrate grain size

Mechanical preparation of metallic samples can remove all the original surface oxides. But this will unavoidably introduce a plastically deformed layer at the surface of metals, because even the finest scratch will create a deformed layer underneath [46]. Based on the work by Samuels [46], a schematic diagram of the surface deformation layer on titanium samples used in this study is provided in Figure 10. The layer at the bottom is the fragmented layer at the surface which contains scratches. A thinner significant deformation layer exists beneath the root of a scratch. The grit number is inversely proportional to the width of the largest scratch, and thus the larger the grit numbers the thinner the deformation zone and the smaller the surface strain.

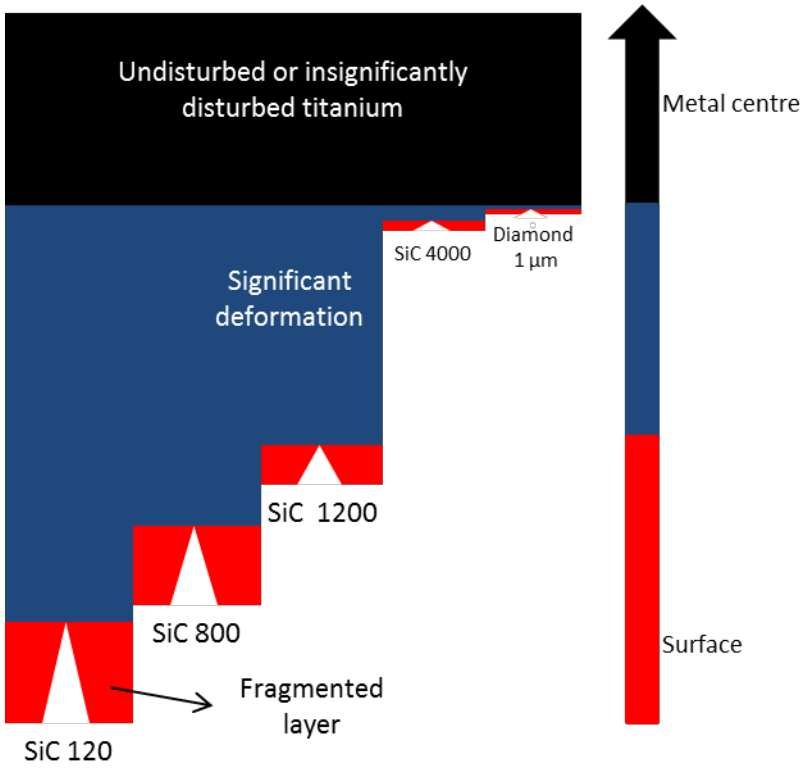

Figure 10 Schematic of titanium surfaces after different mechanical preparation with the fragmented layer and deformation layer depicted [46] .

The fragmented layer consists of severely plastically deformed material. For the 120, 800 and 1200 grit samples, the surfaces are fully covered by scratches, and hence the oxides on those samples formed during anodization should all originate from severely deformed titanium in the fragmented layer. So there is little difference between the CG sample and the HPT sample, because they all have this fragmented layer after mechanical preparation. However HPT and CG samples differ in terms of the characteristics of the material below the fragmented layer and the deformation layer. The difference between TNT layers on the CG and the HPT sample appeared when the grit number increases to 4000 (Figure 6 and Figure 7). This is probably due to the surface containing a thinner deformation layer, so the largely undisturbed materials (the topmost layer in Figure 10) can be turned into oxides. Whilst the severe plastically deformed layers on CG and HPT samples are similar, these samples differ substantially in terms of the material beneath the significantly deformed layer (Figure 2). This can explain why the influence of grain refinement on the growth mechanism and morphology of TNT layers appears for grinding papers of 4000 grit and finer.

4.3.2 The influence of substrate grain size on the TNT morphologies

For an ideal hexagonal arrangement of nanotubes [37] (Figure 11 (a)), d_{bt} is equal to i_d. However, for the CG 4000 grit sample, i_d is larger than d_{bt} by 18.4% (Table 2) and so at the bottom the TNTs do not contact each other (Figure 7 (b), Figure11 (b)). This suggests that those TNTs are still in the initiation stage, because when initiation finishes, TNTs will contact each other. If i_d is smaller than d_{bt}, TNTs are squeezed to each other as shown in Figure11 (c)), and TNTs on the CG800 grit sample shows such a condition (Figure 7 (a)).

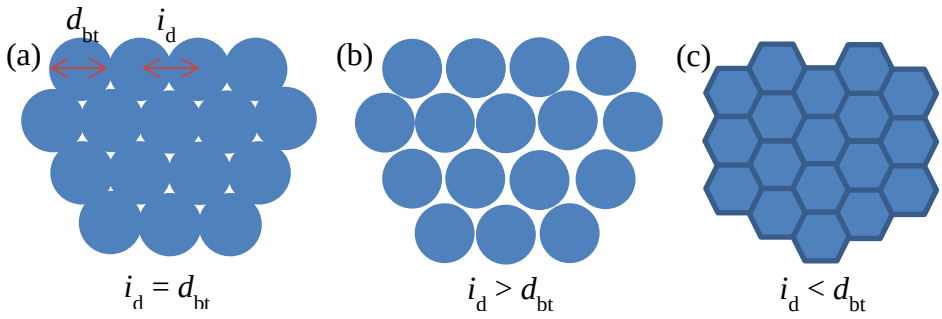

Figure 11 Geometrical parameters of TNT bottom layer, d_{bt} is the external bottom diameter and i_d is the inter-nanotube distance. (a) is the case when $i_d = d_{bt}$, (b) is the case when $i_d > d_{bt}$ and (c) is the case when $i_d < d_{bt.}$

The influences of grain size on TNT layers are shown in the *j-t* curves and the corresponding SEM bottom images. At Stage II there is a competition between Ti oxidation at the Ti/oxide interface and TiO_2 dissolution at the oxide/electrolyte interface. Pores further develop and the effective surface area increases, so *j* subsequently increases until reaching a maximum as a result of the initiation of nanotube growth. A transition from irregular to regular pores, i.e. self-organization, also happens in this stage. Different pores compete for the total available current and only a pore with a sufficiently high current can "survive" [24]. After this natural selection process, a self-organized growth of nanotubes is established. At Stage III, *j* finally achieves a near steady state, the TNT length can increase further by consuming the metallic substrate with fluoride ions partially dissolving the oxide. The *j-t* curve of the HPT30-4000 sample (Figure 5) shows that at about 6000 s the TNT initiation Stage II gives way to the steady growth Stage III, whilst the CG30-4000 sample has not even finished Stage II by the end of the 7200 s experiment. It means the initiation of TNTs on the HPT sample is quicker than on the CG sample. As a result, HPT30-4000 shows a morphology in which TNTs are in contact with each other (Figure 7 (b)) because the HPT sample had already reached Stage III when the experiment stops. On the other hand, the CG30-4000 sample did not finish Stage II

during the experiment, i.e. the growth of TNT layers on it did not reach a stable state, so TNTs had not grown to contact each other. Therefore TNTs on HPT30-4000 contact each other (Figure 7 (b) inset), which is similar to Figure11 (a)), while the bottom morphologies of the CG30-4000 sample (Figure 7 (b)) are similar to the morphologies in Figure11 (b). The faster initiation rate of TNTs on the HPT sample is probably due to a faster oxide dissolution rate on the HPT sample. This consideration can also be applied to 14000 grit processed samples, i.e. on the CG30-14000 sample, the typical three stages in the *j-t* curve are still shown, but with a much weaker "valley" when compared with other CG samples (Figure 5). This suggests that the nucleation rate of TNTs on the CG30-14000 sample is much quicker than the other CG samples. Since oxide dissolution happens quicker on the HPT sample, so its *j-t* curve monotonously dropped and the "valley" almost disappeared. It suggests that the TNT nucleation rate on HPT sample is quicker than that on CG sample, leading to an even smaller d_{bt}.

HPT processing can change the surface oxide in both composition and structure on pure titanium. According to Ref. [47], the natural oxide layer on HPT Ti samples was quite different from that on their CG counterparts in chemical bonding structures. XPS studies revealed that the HPT-processed substrates showed a weakening of the Ti bonding in the TiO_2 on HPT sample, which may lead to the faster dissolution rate of the oxide during the formation of TNT layers.

5 Conclusions

HPT and anodization have been used to modify the bulk and surface properties of titanium for biomedical applications. After 10 turns of HPT under a 3 GPa load, the grains were refined from 10 μm to 140 nm, and the microhardness and the tensile strength were both increased substantially. After anodization on sample surfaces that were mechanically ground

using different procedures, the diameter of TNTs has a complex relationship with the surface roughness. TNTs on 14000 grit diamond paste polished samples possessed the smallest TNT diameters, while samples ground by 4000 grit abrasive papers had the largest TNT diameter. All the samples ground by 1200, 800 and 120 grit abrasive papers showed similar TNT morphologies with intermediate diameters. Analysis using recorded *j-t* curves, SEM and roughness measurements, suggests the titanium surface at nanoscale affects the oxidation rate and thus affect TNT morphologies, whilst roughness on a larger scale (beyond ~100 nm) has little effect. Mechanical preparation significantly affects the morphology of TNTs. HPT processing influences TNT layers only for surface preparations with grit size of 4000 or finer. The oxide dissolution rate was faster for TNT layers on titanium with an UFG microstructure fabricated by HPT processing.

Acknowledgements

This work was supported by a studentship from the Faculty of Engineering and the Environment at the University of Southampton and a scholarship from the China Scholarship Council (CSC). We thank Dr. John Low of the University of Warwick for his support of the anodization experiment.

References

[1] J. Breme, E. Eisenbarth, V. Biehl, Titanium and its Alloys for Medical Applications, Titanium and Titanium Alloys, Wiley-VCH Verlag GmbH & Co. KGaA2005, pp. 423-451.
[2] M. Niinomi, Mechanical properties of biomedical titanium alloys, Materials Science and Engineering: A, 243 (1998) 231-236.
[3] D. Buser, S.F. Janner, J.G. Wittneben, U. Bragger, C.A. Ramseier, G.E. Salvi, 10-year survival and success rates of 511 titanium implants with a sandblasted and acid-etched surface: a retrospective study in 303 partially edentulous patients, Clinical implant dentistry and related research, 14 (2012) 839-851.
[4] R.Z. Valiev, Y. Estrin, Z. Horita, T.G. Langdon, M.J. Zehetbauer, Y.T. Zhu, Producing bulk ultrafine-grained materials by severe plastic deformation, JOM, 58 (2006) 33-39.
[5] A.V. Sergueeva, V.V. Stolyarov, R.Z. Valiev, A.K. Mukherjee, Advanced mechanical properties of pure titanium with ultrafine grained structure, Scripta Mater, 45 (2001) 747-752.

[6] G. Balasundaram, C. Yao, T.J. Webster, TiO_2 nanotubes functionalized with regions of bone morphogenetic protein-2 increases osteoblast adhesion, Journal of biomedical materials research. Part A, 84 (2008) 447-453.
[7] L. Peng, M.L. Eltgroth, T.T.J. La, C.A. Grimes, T.A. Desai, The effect of TiO_2 nanotubes on endothelial function and smooth muscle proliferation, Biomaterials, 30 (2009) 1268-1272.
[8] L. Peng, A.J. Barczak, R.A. Barbeau, Y. Xiao, T.J. LaTempa, C.A. Grimes, T.A. Desai, Whole Genome Expression Analysis Reveals Differential Effects of TiO_2 Nanotubes on Vascular Cells, Nano Letters, 10 (2009) 143-148.
[9] K.S. Brammer, S. Oh, J.O. Gallagher, S. Jin, Enhanced Cellular Mobility Guided by TiO_2 Nanotube Surfaces, Nano Letters, 8 (2008) 786-793.
[10] J. Park, S. Bauer, K. von der Mark, P. Schmuki, Nanosize and vitality: TiO_2 nanotube diameter directs cell fate, Nano Letters, 7 (2007) 1686-1691.
[11] J. Park, S. Bauer, P. Schmuki, K. von der Mark, Narrow Window in Nanoscale Dependent Activation of Endothelial Cell Growth and Differentiation on TiO_2 Nanotube Surfaces, Nano Letters, 9 (2009) 3157-3164.
[12] J.P. Spatz, Cell–Nanostructure Interactions, Nanobiotechnology, Wiley-VCH Verlag GmbH & Co. KGaA2005, pp. 53-65.
[13] A.W. Tan, B. Pingguan-Murphy, R. Ahmad, S.A. Akbar, Review of titania nanotubes: Fabrication and cellular response, Ceramics International, 38 (2012) 4421-4435.
[14] M. Nie, C. Wang, M. Qu, N. Gao, J. Wharton, T. Langdon, The corrosion behaviour of commercial purity titanium processed by high-pressure torsion, Journal of Materials Science, 49 (2014) 2824-2831.
[15] J.H. Gao, S.K. Guan, Z.W. Ren, Y.F. Sun, S.J. Zhu, B. Wang, Homogeneous corrosion of high pressure torsion treated Mg–Zn–Ca alloy in simulated body fluid, Materials Letters, 65 (2011) 691-693.
[16] H. Nakano, H. Yamaguchi, Y. Yamada, S. Oue, I.-J. Son, Z. Horita, H. Koga, Effects of High-Pressure Torsion on the Pitting Corrosion Resistance of Aluminum-Iron Alloys, Materials Transactions, 54 (2013) 1642-1649.
[17] A. Korchef, A. Kahoul, Corrosion Behavior of Commercial Aluminum Alloy Processed by Equal Channel Angular Pressing, International Journal of Corrosion, 2013 (2013) 11.
[18] J. Dong, J. Han, X. Ouyang, W. Gao, How voltage dictates anodic TiO_2 formation, Scripta Materialia, 94 (2015) 32-35.
[19] J.M. Macak, H. Tsuchiya, L. Taveira, S. Aldabergerova, P. Schmuki, Smooth Anodic TiO_2 Nanotubes, Angewandte Chemie International Edition, 44 (2005) 7463-7465.
[20] J.M. Macák, H. Tsuchiya, P. Schmuki, High-Aspect-Ratio TiO_2 Nanotubes by Anodization of Titanium, Angewandte Chemie International Edition, 44 (2005) 2100-2102.
[21] S.P. Albu, A. Ghicov, J.M. Macak, P. Schmuki, 250 μm long anodic TiO_2 nanotubes with hexagonal self-ordering, Physica Status Solidi (RRL) – Rapid Research Letters, 1 (2007) R65-R67.
[22] M. Paulose, K. Shankar, S. Yoriya, H.E. Prakasam, O.K. Varghese, G.K. Mor, T.A. Latempa, A. Fitzgerald, C.A. Grimes, Anodic Growth of Highly Ordered TiO_2 Nanotube Arrays to 134 μm in Length, The Journal of Physical Chemistry B, 110 (2006) 16179-16184.
[23] W. Wei, S. Berger, C. Hauser, K. Meyer, M. Yang, P. Schmuki, Transition of TiO_2 nanotubes to nanopores for electrolytes with very low water contents, Electrochemistry Communications, 12 (2010) 1184-1186.
[24] L.V. Taveira, J.M. Macák, H. Tsuchiya, L.F.P. Dick, P. Schmuki, Initiation and Growth of Self-Organized TiO2 Nanotubes Anodically Formed in $NH_4F/(NH_4)_2SO_4$ Electrolytes, Journal of The Electrochemical Society, 152 (2005) B405-B410.
[25] J.M. Macak, M. Jarosova, A. Jäger, H. Sopha, M. Klementová, Influence of the Ti microstructure on anodic self-organized TiO_2 nanotube layers produced in ethylene glycol electrolytes, Applied Surface Science, 371 (2016) 607-612.
[26] S. Leonardi, V. Russo, A. Li Bassi, F. Di Fonzo, T.M. Murray, H. Efstathiadis, A. Agnoli, J. Kunze-Liebhauser, TiO_2 nanotubes: interdependence of substrate grain orientation and growth rate, ACS applied materials & interfaces, 7 (2015) 1662-1668.
[27] K. Lu, Z. Tian, J.A. Geldmeier, Polishing effect on anodic titania nanotube formation, Electrochimica Acta, 56 (2011) 6014-6020.

[28] A. Apolinario, C.T. Sousa, J. Ventura, J.D. Costa, D.C. Leitao, J.M. Moreira, J.B. Sousa, L. Andrade, A.M. Mendes, J.P. Araujo, The role of the Ti surface roughness in the self-ordering of TiO_2 nanotubes: a detailed study of the growth mechanism, Journal of Materials Chemistry A, 2 (2014) 9067-9078.
[29] M. Adachi, Y. Murata, I. Okada, S. Yoshikawa, Formation of Titania Nanotubes and Applications for Dye-Sensitized Solar Cells, Journal of The Electrochemical Society, 150 (2003) G488-G493.
[30] A.S. Arico, P. Bruce, B. Scrosati, J.M. Tarascon, W. Van Schalkwijk, Nanostructured materials for advanced energy conversion and storage devices, Nature Materials, 4 (2005) 366-377.
[31] B. O'Regan, M. Gratzel, A low-cost, high-efficiency solar cell based on dye-sensitized colloidal TiO2 films, Nature, 353 (1991) 737-740.
[32] I.D. Kim, A. Rothschild, B.H. Lee, D.Y. Kim, S.M. Jo, H.L. Tuller, Ultrasensitive chemiresistors based on electrospun TiO_2 nanofibers, Nano Letters, 6 (2006) 2009-2013.
[33] C. Xu, Z. Horita, T.G. Langdon, The evolution of homogeneity in an aluminum alloy processed using high-pressure torsion, Acta Materialia, 56 (2008) 5168-5176.
[34] R.Z. Valiev, R. Islamgaliev, I. Alexandrov, Bulk nanostructured materials from severe plastic deformation, Prog. Mater. Sci., 45 (2000) 103-189.
[35] J.M. Macak, H. Tsuchiya, A. Ghicov, K. Yasuda, R. Hahn, S. Bauer, P. Schmuki, TiO_2 nanotubes: Self-organized electrochemical formation, properties and applications, Current Opinion in Solid State and Materials Science, 11 (2007) 3-18.
[36] G.K. Mor, O.K. Varghese, M. Paulose, K. Shankar, C.A. Grimes, A review on highly ordered, vertically oriented TiO_2 nanotube arrays: Fabrication, material properties, and solar energy applications, Solar Energy Materials and Solar Cells, 90 (2006) 2011-2075.
[37] P. Roy, S. Berger, P. Schmuki, TiO2 Nanotubes: Synthesis and Applications, Angewandte Chemie-International Edition, 50 (2011) 2904-2939.
[38] A.A. Popov, I.Y. Pyshmintsev, S.L. Demakov, A.G. Illarionov, T.C. Lowe, A.V. Sergeyeva, R.Z. Valiev, Structural and mechanical properties of nanocrystalleve titanium processed by severe plastic deformation, Scripta Materialia, 37 (1997) 1089-1094.
[39] M.J. Starink, X. Cheng, S. Yang, Hardening of pure metals by high-pressure torsion: A physically based model employing volume-averaged defect evolutions, Acta Materialia, 61 (2013) 183-192.
[40] R.Z. Valiev, N.A. Enikeev, X. Sauvage, Superstrength of nanostructured alloys produced by SPD processing, Journal of Physics: Conference Series, 291 (2011) 012029.
[41] V.V. Stolyarov, Y.T. Zhu, T.C. Lowe, R.Z. Valiev, Microstructure and properties of pure Ti processed by ECAP and cold extrusion, Materials Science and Engineering: A, 303 (2001) 82-89.
[42] X.G. Qiao, N. Gao, M.J. Starink, A model of grain refinement and strengthening of Al alloys due to cold severe plastic deformation, Philosophical Magazine, 92 (2012) 446-470.
[43] X.G. Qiao, M.J. Starink, N. Gao, Hardness inhomogeneity and local strengthening mechanisms of an Al1050 aluminium alloy after one pass of equal channel angular pressing, Materials Science and Engineering: A, 513–514 (2009) 52-58.
[44] A. Valota, M. Curioni, D.J. Leclere, P. Skeldon, P. Falaras, G.E. Thompson, Influence of Applied Potential on Titanium Oxide Nanotube Growth, Journal of The Electrochemical Society, 157 (2010) K243-K247.
[45] D. Regonini, A. Satka, A. Jaroenworaluck, D.W.E. Allsopp, C.R. Bowen, R. Stevens, Factors influencing surface morphology of anodized TiO2 nanotubes, Electrochimica Acta, 74 (2012) 244-253.
[46] L.E. Samuels, Metallographic Polishing by Mechanical Methods, 4th Edition, ASM International 2003.
[47] S. Faghihi, A.P. Zhilyaev, J.A. Szpunar, F. Azari, H. Vali, M. Tabrizian, Nanostructuring of a Titanium Material by High-Pressure Torsion Improves Pre-Osteoblast Attachment, Advanced Materials, 19 (2007) 1069-1073.